Development of an Elementary Climate Model: Two-Layer Cellular Case

Introduction

The recent gradual increase in Earth's average temperature[1] is generating intense interest in both public and scientific circles. It is important that physicists understand the basic energetics in climatology. While excellent climatology texts such as Hartmann's[2] exist, materials generally available to the undergraduate physics major and instructor lack a systematic physical treatment and an unavoidable terminology barrier exists. The comprehensive and readable work of Peixoto and Oort,[3] written by and for physicists, is at a level too demanding for introductory study. We concentrate solely on some aspects of the basic energy transfer to establish a level suitable for undergraduate teaching; more sophisticated treatments do exist.[4–7]

Despite the complexities of the real atmosphere, the global average temperature of 288 K (Ref. 2, p. 2) may be estimated with remarkably few modifications of the classic homogeneous blackbody model of Earth.[2,8–11] One purpose of developing this article has been to build on our earlier elementary model[9] as realistically as possible, retaining both a physics style and a reasonable mathematical and computational level. We thought it would be of interest to see whether the two-layer model of the energy fluxes could be employed on a regional basis, for which we consider Earth's surface covered by a layer of 864 noninteracting cells. Here we will show that it does appear to be a consistent theory that can provide certain insights. In particular, we find that the cellular radiative energy transports clearly dominate the cellular nonradiative energy flux. We show that this flux has a strong systematic dependence on latitude and time of year. Thus, for this article we wish to avoid using a more precise radiative model of the atmosphere. Also, all heat transmission through the earth's surface is neglected. This precludes a quantitative prediction of the phase difference between the cyclical variations of the solar flux and the surface temperature.

We first briefly review the two-layer model in order to set up notation. In our earlier work[9] the two layers of the Arrhenius model were called, informally, the atmosphere and the surface. Except for one nonradiative flux S_{NR}, all energy transfers were modeled as radiative. The model makes use of the fact that the incoming solar radiation and the outgoing terrestrial radiation occupy distinct spectral regions called respectively, for convenience, UV and IR. The upper layer, at temperature T_A, has a UV reflectivity and absorptivity, r_A and a, respectively, and an IR absorptivity ε. The symbols a and ε are used here in place of f and g in the original article but all other notation is preserved. The surface, at temperature T_E, has a UV reflectivity r_S and is assumed to absorb all incident IR. The solar radiation has a flux $S_0 = 342$ W/m^2 when averaged over time and over the surface of the earth. When the UV radiation hits the upper layer, a part r_A is reflected and the part that enters the layer is $(1-r_A)$. Of this part, $a(1-r_A)$ is absorbed. In this first pass, the surface therefore receives $(1-r_A)(1-a)$, of which r_S is reflected, leaving $(1-r_A)(1-a)(1-r_S)$ as the fraction of original incident solar flux to be absorbed at the surface. Following this logic, a diagram can be constructed showing all the fractions of absorbed and reflected radiation including the term S_{NR} for nonradiative energy transfer (Fig. 94.63). When multiple reflections are included, a factor $k_M = \left(1 - r_A r_S\right)^{-1}$ appears in terms involving reflections between the surface and atmosphere. The nonradiative flux S_{NR}, which served as an arbitrary model parameter in the global calculation, will be seen to play a much greater role in the current work.

The energy-balance equations for the upper and surface layers take the form

$$2\varepsilon S_A - \varepsilon S_E = AS_0 + S_{\mathrm{NR}} \tag{1a}$$

and

$$-\varepsilon S_A + S_E = BS_0 - S_{\mathrm{NR}}, \tag{1b}$$

respectively. These equations express net incoming UV and nonradiative flux on the right-hand sides and net outgoing IR flux on the left. Here S_A and S_E are defined as the ideal Stefan–Boltzmann fluxes $S_A = \sigma T_A^4$ and $S_E = \sigma T_E^4$, where $\sigma = 5.67 \times 10^{-8}$ W/m^2 K^{-4}. The quantities A and B correspond to the fractions of S_0 ultimately absorbed by the atmosphere and

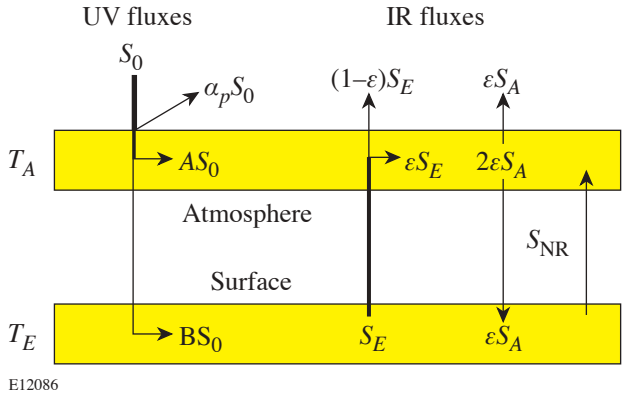

Figure 94.63
Movement of radiative and nonradiative energy in the two-layer scheme. Horizontal arrows indicate deposition in the layer. Lighter arrows represent radiation that is either reflected or passed through a layer unabsorbed. Multiple reflections of UV radiation are accounted for by the factor k_M in Eqs. (1a) and (1b) in the text. The factors α_p, A, and B are the overall fractions of S_0 that are reflected, absorbed by the upper layer, and absorbed by the lower layer, respectively. Other symbols are defined in the text.

surface, respectively,

$$A = a(1-r_A) + ak_M(1-r_A)^2\,(1-a)r_S \qquad (2a)$$

and

$$B = k_M(1-r_A)(1-r_S)(1-a) \qquad (2b)$$

Global and time averages of all the parameters are inserted, and Eqs. (1) are easily solved for S_A and S_E, from which temperatures T_A and T_E are then obtained. This original model was used to investigate broadly the effect of non-solar-related energy sources at the surface.

The following sections (1) extend the model by introducing coarsely grained surface features and locally time averaged fluxes in 864 noninteracting cells; (2) compute and discuss zonal (latitudinal) averages; and (3) summarize and discuss the limitations of the model and possibilities for its further development.

Cellular Model

1. Rationale and Design

We choose the grid scheme used by Hansen *et al.*[12] in which the earth's surface is divided into 864 cells of dimension 8° × 10° (latitude by longitude). We then assume that Eqs. (1) are satisfied within each cell. The next step is to extend the computations from globally time-averaged to locally time-averaged parameters. For each of the 864 cells, the land fraction and the annually averaged parameters for observed total cloud cover fraction, calculated incoming annual average solar radiation, and land and sea reflectivities are stored. All parameters are determined at the center of the cell, and the values are applied to the entire area of the cell. The energy-balance equations are then solved at each location. For comparison to global values, the local values are weighted by fractional cell area and summed. Our model does not take into account changes in atmospheric components, the parameters' temperature dependence,[11] or any geothermal variations.

All programming is done using MATLAB™, an array-based language with simple commands. In the MATLAB environment, each computation is performed simultaneously on each cell in an identical manner. A very useful source for MATLAB programming styles is the Appendix of a text by Borse.[13]

Before solving the energy-balance equations for the temperatures and emissions of the two layers, the input parameters must be specified. These values have been gathered from different sources. The land fraction $f_{land}(n)$ is taken directly from Hansen *et al.*[12] It is shown by the contours in Fig. 94.64, which establishes the scale and resolution of subsequent maps.

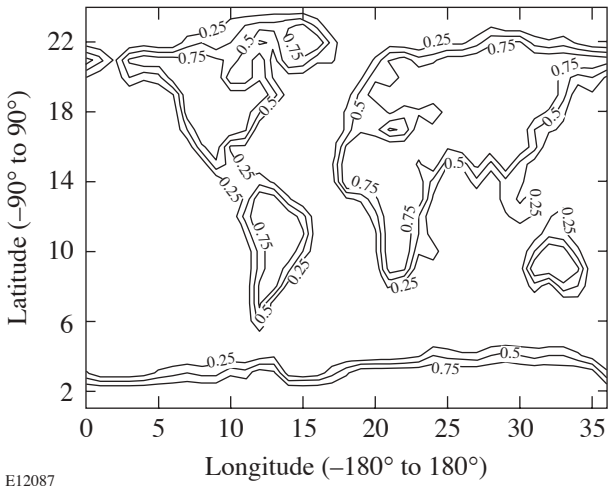

Figure 94.64
Global land fraction plotted with contours at 0.25, 0.5, and 0.75. This map may be used as a template in the study of Figs. 94.66, 94.67, and 94.69. It also gives a good indication of the resolution afforded by our 864-cell calculations. Horizontal axis: ticks correspond to centers of 10° cells located (centered) at longitudes −180°(1), −170°(2), ..., 0°(19), ..., +170°(36). Vertical axis: ticks correspond to centers of 8° cells at latitudes −84°(2), −76°(3), ..., −4°(12), +4°(13), ..., +84°(23). The bottom and top rows correspond to centers of 2° cells at −89°(1) and +89°(24), respectively.

The 18-year-average annual cloud fraction coverage was taken from data collected by satellites from 1983 to 2001 under the International Satellite Cloud Climatology Project.[14] Similarly, surface reflectivities (r_S) were estimated by using the ISCCP surface reflectivities in coordination with Table 4.2 in Hartmann.[2] Hartmann specifies albedo ranges and typical values for distinct land types. Table 94.II shows the land types, albedo ranges, and typical albedo values. The estimates of r_S are shown in Table 94.III.

It might appear that a serious approximation is being made in neglecting net annual lateral transport of energy. Lateral heat flows, however, will be effectively redirected into a vertical heat flux; the quantity S_{NR} will contain this contribution. Consider, for example, a horizontal wind, carrying water vapor from one cell to the next. When the vapor precipitates in the form of rain, it releases latent energy. That energy release contributes to the vertical energy balance in the (receptor) cell. This energy enters "horizontally" into the cell. Similarly, in some nearby cell, some vertical energy flux went into evaporation, and that cell suffers an energy loss if the water vapor is transported out of the cell. Since our cells are large, we do not expect the horizontal energy transport to cover more than one or two cells, for local disturbances. Consequently there may be a correlation between a loss of S_{NR} in one cell and a gain in S_{NR} in a nearby cell. The annual latitude dependence of S_{NR}, which will be discussed in the last section, may well be made up of such transport contributions. A less obvious but very significant assumption is that the theory continues to work at latitudes having long periods of low solar irradiance, when cloud cover may vary significantly between polar winter and summer periods. This requires negative values of S_{NR} to maintain flux

Table 94.II: Land types and their associated albedo ranges (in percentages) deduced from a map [Fig. 5.14, by Dickinson (Ref. 18); Table 4.2 by Hartmann (Ref. 2)].

Land type (Dickinson)	Land type (Hartmann)	Albedo range	Typical value
Tundra and desert	Dry soil/desert	20–35	30
Grass and shrub	Short green vegetation	10–20	17
Crop	Dry vegetation	20–30	25
Wetland and irrigated	Short green vegetation	10–20	17
Evergreen tree	Coniferous forest	10–15	12
Deciduous tree	Deciduous forest	15–25	17

Table 94.III: Corrected values for land and sea reflectivities in the high latitudes (see text). A negative latitude corresponds to the southern hemisphere. For −76° to −89° r_{land} is set at 0.6 because of the year-round Antarctic ice. The latitude −68° reflectivity is set slightly lower than Antarctica as a result of a lack of permanent ice. In latitudes 68° to the north pole, r gradually increases, taking seasonal snow and ice into account. r_{sea} at 60° and −60° is set at 0.3 to avoid a sharp jump from water set at 0.1 in the mid-latitudes to the higher polar values for ice and snow cover. These values are rough estimates for partial and seasonal snow and ice cover. Fresh snow can have an albedo up to 0.9, old, melting snow up to 0.65, and sea ice without snow cover up to 0.4 (see Ref. 2, Table 4.2, p. 88). Values not shown (—) are longitude dependent and are taken directly from satellite data in detail.

Latitude (°)	−89	−84	−76	−68	−60	−52 to 52	60	68	76	84	89
r (land)	0.6	0.6	0.6	0.55	—	—	—	0.4	0.5	0.55	0.6
r (sea)	0.6	0.6	0.6	0.55	0.3	—	0.3	0.4	0.5	0.55	0.6

balance. Negative values of S_{NR} may represent fluxes from a missing reservoir layer, which is planned for a future refinement of the model.

2. Cellular Values of Parameters

The value of a parameter g that depends on the choice of cell will be written $g(n)$, where, unless otherwise specified, n is an arbitrarily assigned cell number. To calculate the incoming solar radiative flux to a cell, we use astronomical definitions and notations to track the sun's position relative to a cell's midpoint every two weeks throughout the year. The incident radiation is the solar radiation at the distance to the earth, 1368 W/m^2 multiplied by the sine of $H(n)$, where $H(n)$ is the angle of the sun from the horizon of the surface area in cell n,

$$S_0(n) = 1368 \sin H(n,t,t') \left(\mathrm{Wm}^{-2}\right). \tag{3}$$

Here (see Appendix and Ref. 2, pp. 29–31 and 347–349)

$$\sin H(n,t,t') = \sin\delta(t')\sin\beta(n) + \cos\delta(t')\cos\beta(n)\cos t, \tag{4}$$

where β is the latitude, δ is the sun's declination angle, t' is the time elapsed since the vernal equinox, and t is the hour angle. During the average over 24-h periods, the angle t is limited by sunrise and sunset conditions, i.e., there is no contribution when sin H is negative. The annual average of S_0 as a function of latitude computed from Eq. (3) is plotted in Fig. 94.65,

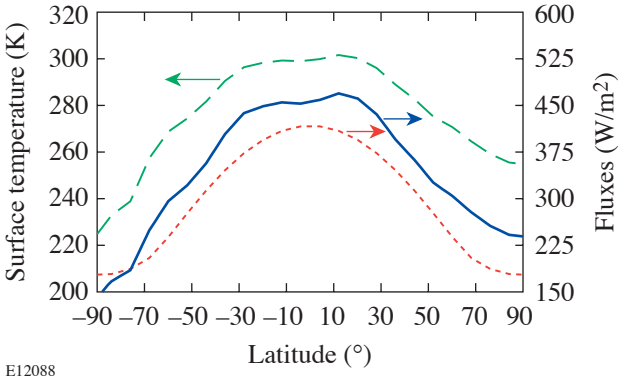

Figure 94.65
Average annual insolation (lower curve, right-hand scale), outward infrared flux at the surface (solid curve, right-hand scale), and surface temperature (upper curve, left-hand scale) as a function of latitude. The latter two are latitude averages based on satellite data.[15]

along with the observed S_E and T_E. Equation (3) is adequate for the purposes of our average annual model. Monthly averages require a slight correction resulting from Earth's orbital eccentricity (see, e. g., Hartmann[2]). The annual average solar irradiance ranges from a minimum of 176 W/m^2 at the poles to 416 W/m^2 at the equator, with a global annual average of 342 W/m^2.

The UV parameters A and B [Eqs. (2a) and (2b)] also become cell dependent. There are three relevant cell-varying parameters, the UV reflectivities and the absorptivity of the cloud layer. The surface reflectivity $r_S(n)$ of cell n is taken from sea and land reflectances weighted by the corresponding surface-type fractions,

$$r_s(n) = f_{\mathrm{land}}(n) r_{\mathrm{land}} + \left[1 - f_{\mathrm{land}}(n)\right] r_{\mathrm{sea}}\,. \tag{5}$$

This formula was used only in high-latitude regions ($|\mathrm{lat}| \geq 60°$). Remaining reflectivities came from ISCCP data.[14,15] The atmospheric reflectivities are similarly found to be

$$r_A(n) = f_{\mathrm{cloud}}(n)\, r_{\mathrm{cloud}} + \left[1 - f_{\mathrm{cloud}}(n)\right] r_{\mathrm{clear}}, \tag{6}$$

where the clear air albedo (r_{clear}) can be assumed as 0.15 (Ref. 2, page 75). The planetary albedo $\alpha_P(n)$ is the fraction of original incident UV that leaves the system. On our model [see Ref. 5, Eq. (B3)] it is given by

$$\alpha_P(n) = r_A(n) + k_M(n)\left[1 - a(n)\right]^2 \left[1 - r_A(n)\right]^2 r_S(n), \tag{7}$$

which depends upon two unknowns: $a(n)$, the atmospheric UV absorptivity, and r_{cloud} [through r_A, Eq. (6)]. For absorptivity, the expression corresponding to (6) is

$$a(n) = f_{\mathrm{cloud}}(n)\; a_{\mathrm{cloud}} + \left[1 - f_{\mathrm{cloud}}(n)\right] a_{\mathrm{clear}}. \tag{8}$$

If we assume that clear air absorbs no UV radiation, we have

$$a(n) \cong f_{\mathrm{cloud}}(n)\, a_{\mathrm{cloud}}. \tag{9}$$

To determine r_{cloud} and a_{cloud}, we impose a set of reasonable planetary albedo values [Ref. 2, Fig. 2.9(a), p. 33] as a constraint upon Eq. (7). Values of r_{cloud} and a_{cloud} were varied at intervals of 0.01 until we had the greatest number of matches

with the known $\alpha_P(n)$. With this bare minimum of free parameters, a match to observed values occurred in 711 of the 864 cells. Most of the unmatched (meaning more than 15% difference from the Hartmann) values were near the poles. The resulting $r_{\text{cloud}} = 0.27$ and $a_{\text{cloud}} = 0.06$ are in reasonable agreement with the parameters found in Ref. 9. These produce not only a good localized match but also give the commonly accepted global planetary albedo of 0.30 when averaged. Once adopted, these values of r_{cloud} and a_{cloud} are not changed in the course of the calculations.

The cellular IR absorptivity $\varepsilon(n)$, which is also the cellular IR emissivity, is taken to have the same form as the UV absorptivity, Eq. (8). Parameters used were $\varepsilon_{\text{cloud}} = 1$ and $\varepsilon_{\text{clear}} = 0.90$.

Application of the Model

1. Predicting $T_E(n)$

We now generalize Eqs. (1a) and (1b) to the cellular case:

$$2\varepsilon S_A(n) - \varepsilon S_E(n) = A(n)\,S_0(n) + S_{\text{NR}}(n) \qquad (10a)$$

and

$$-\varepsilon S_A(n) + S_E(n) = B(n)\,S_0(n) - S_{\text{NR}}(n). \qquad (10b)$$

$A(n)$ and $B(n)$ are given by equations identical to Eqs. (2a) and (2b) in which certain parameters are made cell dependent, as discussed above.

Our first attempt with the cellular model was a direct 864-cell extension of the methodology of the earlier one-cell or one-dimensional two-layer model. We refer to this application of the model as "T_E predictive." We allowed the annual average value of $S_{\text{NR}}(n)$ to depend on land and sea fraction and took it to be proportional to the solar input, as follows:

$$S_{\text{NR}}(n) = \left[0.03 f_{\text{land}}(n) + 0.16 f_{\text{sea}}(n)\right] \cdot S_0(n). \qquad (11)$$

From the solution of each pair of Eqs. (10a) and (10b) for $S_E(n)$, $T_E(n)$ was calculated on the basis of the assumed $S_{\text{NR}}(n)$. The numerical coefficients in Eq. (11) were chosen by an extensive search of parameter space to produce the observed global average temperatures ($T_E = 288$ K, $T_A = 250$ K). This flux has a global average of 42.3 W/m^2, an improvement on the one-dimensional model[9] in that the latter had been unable to accommodate *any* non-zero average S_{NR} without compromising other assumed input parameters. We emphasize that the only completely arbitrary parameters in the fit were the two numerical coefficients in Eq. (11). We consider this remarkable; it endorses the general reasonableness of the elementary two-temperature model for individual cells. The form of Eq. (11) also suggests a global asymmetry in the distribution of S_{NR}. We will return to this later.

The preliminary cell results are shown in Fig. 94.66(a) and are compared with measured values [satellite data;[15]

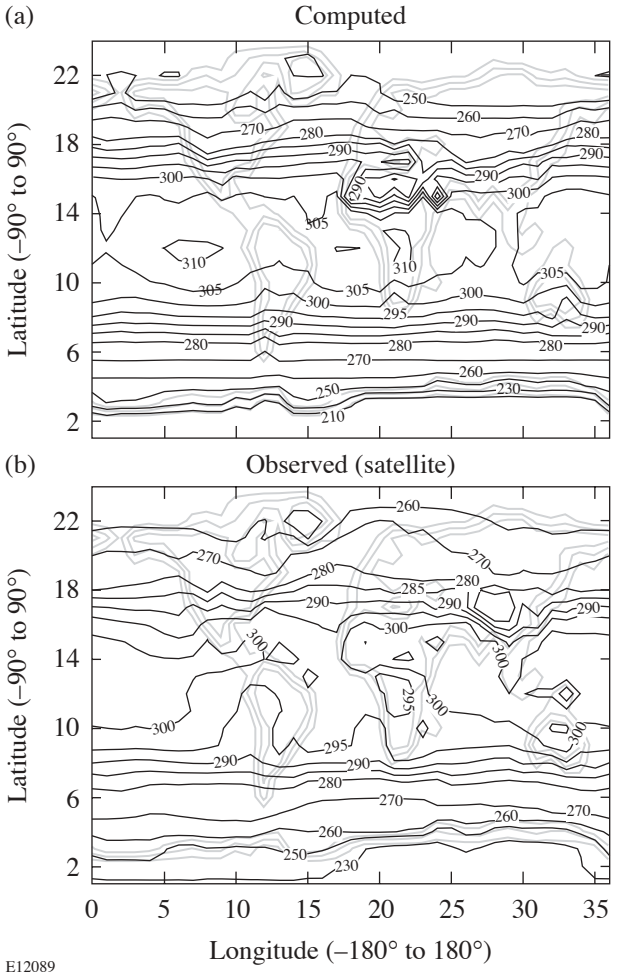

Figure 94.66
(a) Computed "T_E-predictive mode" surface temperatures (in K) using a direct cellular extension of the elementary model of Ref. 9, as described in the text. The average nonradiative flux is 40 W/m^2 and the average surface temperature is 288 K. (b) Observed surface temperatures, defined as those obtained by satellite,[15] with an average of 288 K. (See the caption of Fig. 94.64 for the key to the axes.)

Fig. 94.66(b)]. These diagrams show how a set of calculated locally determined temperatures [Fig. 94.66(a)] having the correct global average may disagree significantly from observed local values [Fig. 94.66(b)] having the same global average. While this is not the least bit surprising, a comparison of the two parts of Fig. 94.66 provides a qualitative evaluation of the errors that occur in the making of simple models. The agreement is closer than one might reasonably expect from simplistic models but the determined set is far from unique.

2. Predicting $S_{NR}(n)$

Because of the difficulty choosing the coefficients of Eq. (11) to produce a match with observations [Figs. 94.66(a) and 94.66(b)], we made a major change in operational procedure. The linear Eqs. (1a) and (1b) or (10a) and (10b) lend themselves equally to computing any two of the quantities S_{NR}, S_A, and S_E, given the third one and S_0 as an input. Therefore, instead of adjusting the value of S_{NR} to predict observed local surface temperatures, we did the opposite: taking $T_E(n)$ as a known input parameter from ISCCP satellite data[11] and $S_0(n)$ from Eq. (3), we used the balance equations to calculate $S_A(n)$ and $S_{NR}(n)$. This "S_{NR}-predictive" mode of calculation is accomplished most easily by combining the two flux Eqs. (10a) and (10b):

$$S_{NR}(n) = \left[A(n) + 2B(n)\right] S_0(n) - (2-\varepsilon) S_E(n). \quad (12)$$

Recall that $S_E(n) = \sigma T_E(n)^4$. Eliminating S_E from (10a) and (10b) results in the companion equation for S_A:

$$\varepsilon(2-\varepsilon) S_A(n)$$

$$= \left[A(n) + \varepsilon B(n)\right] S_0(n) + (1-\varepsilon) S_{NR}(n). \quad (13)$$

The results for the annual average of $S_{NR}(n)$, calculated from the observed surface temperature $T_E(n)$, are shown in Fig. 94.67(a). $S_{NR}(n)$ and $S_A(n)$ have global averages of 64 and 236 W/m^2 (the latter corresponding to T_A = 254 K), respectively. In the earlier noncellular model,[9] the highest value of S_{NR} that could be obtained without unreasonable parameters was 40 W/m^2, and in the above T_E-predictive mode it was 42.3 W/m^2, so the S_{NR}-predictive mode result 64 W/m^2 represents a further improvement. The generally quoted global average of S_{NR} is 102 to 105 W/m^2.[16,17] $S_{NR}(n)$ appears to be most negative at the higher latitudes and most positive near the equator. A negative value of $S_{NR}(n)$ corresponds to nonradiative energy transfer from the atmospheric layer to the surface layer or a lateral flow into the cell, as discussed earlier.

A distinctive feature of our results is the prominent drop of S_{NR} in the regions of the Sahara and Saudi Arabia [Fig. 94.67(a), at matrix elements (20–25, 14–16)]. Its cause is a confluence of strong effects on the two terms in Eq. (12): relatively high surface reflectivity and low cloud cover, which reduce the first term, and relatively high temperature, which increases the absolute value of the (negative) second

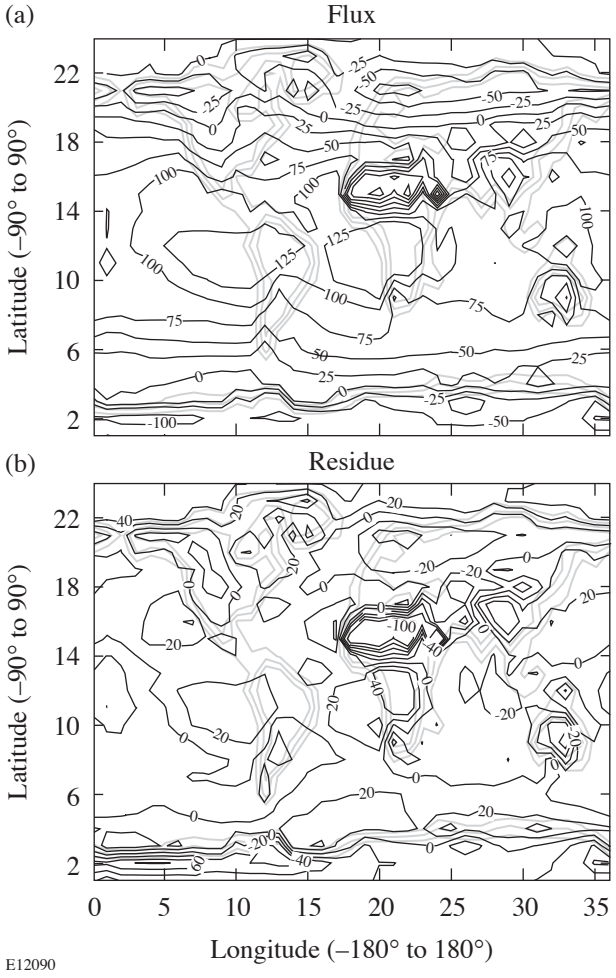

Figure 94.67
(a) Computed "S_{NR}-predictive mode" nonradiative flux $S_{NR}(n)$ (in W/m^2) using the cellular model but with surface temperatures as input. (b) $\delta S_{NR}(n)$, the residue after subtracting the annual average value of $S_{NR}(n)$ as a function of latitude [see Eq. (16)]. The one region of large residuals corresponds to the Sahara desert region. (See the caption of Fig. 94.64 for the key to the axes.)

term. A similar but milder dip appears in the eastern region of Australia.

Figures 94.67 and 94.68 reveal a possible smooth dependence of $S_{NR}(n)$ on latitude. Figure 94.67(b) shows the residues $\delta S_{NR}(n)$ after latitude averages are removed, as discussed in the next section.

3. The Zonal Average of S_{NR}

"Zonal" averages are made over cells lying within zones having the same latitude. Following convention,[18] we denote zonal averages by angular brackets $\langle ... \rangle$. If the area of cell $n = (p,q)$ is $A(p,q)$, where p is the latitude cell index and q is the longitude cell index, we have, for example,

$$\langle S_{NR}(p) \rangle = \frac{1}{A(p)} \sum_q A(p,q) S_{NR}(p,q), \qquad (14)$$

where $A(p)$ is the total area of zone p,

$$A(p) = \sum_q A(p,q). \qquad (15)$$

For convenience the latitude index p will be converted into the latitude β, measured in degrees, at the center of the cell and we will write, again for example, $S_{NR}(\beta) = \langle S_{NR}(p) \rangle$.

The zonal averages $S_{NR}(\beta)$ are shown explicitly in Fig. 94.68, where a very regular latitude dependence emerges clearly. Indeed, $S_{NR}(\beta)$ can be represented to within ±9 W/m^2 by

$$S_{NR}^{fit}(\beta) = 40 + 80 \cos 2(\beta + \Delta) - 10 \sin 6|\beta|, \qquad (16)$$

with $\Delta = 5°$. In Fig. 94.68 the residuals between $S_{NR}(\beta)$ and its fit are also shown. When this zonal average is removed from the cellular results of Fig. 94.67(a), the residuals [Fig. 94.67(b)] are obtained. They are noteworthy for their general smoothness and for their relatively small size, which is of the order of 5%–10% of the solar input at the surface.

It is not surprising that $S_{NR}(\beta)$ has an asymmetry between the northern and southern hemispheres. In retrospect we see that the *ad hoc* form, Eq. (11), used in the T_E-predictive calculation, was biased toward the southern hemisphere, where

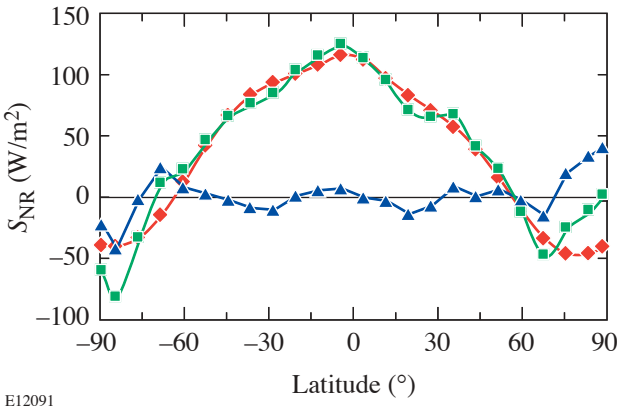

Figure 94.68
Distribution of S_{NR} by latitude. Squares represent the "experimental" values based on our model, and diamonds are the numerical fit, Eq. (16). Triangles are the residuals.

the sea fraction is dominant. Figure 94.69 shows the 18-year-average surface reflectivity in months 1 and 7 (Ref. 10), giving further insight into the peculiarities of S_{NR}. The reflectivities are slightly higher in the northern temperate zone than in the southern. In the polar regions, the times of greater solar irradiance may not occur when the surface reflectance is at its average value. Indeed, the polar regions are generally rather anomalous. We have not concerned ourselves too much with them because the model, generally limited to dealing with annual averages, lacks the ability to describe accurately the effect of Arctic and Antarctic nights in which $S_0(n) = 0$. There is some seasonal variation in the cloud cover data, which may be responsible for the fact that the interesting term $-10 \sin 6|\beta|$ does not hold in the polar regions. One is tempted to speculate on the origin of the sinusoidal term: the insolation does not have a pure $\cos\beta$ dependence because of the inclination of Earth's axis to the plane of its orbit, and Hadley cells[19] may play a role in it.

The existence of extensive databases provides the student an opportunity to explore many other effects through the medium of this theory. As an example, we have used data from ISCCP[14] consisting of averages of the measured parameters at each month over an 18-year period. For each month, the average $S_{NR}(\beta,t)$ was calculated and compared to $S_{NR}(\beta)$ by looking at the difference between the two. This difference also appears to follow a trend that is most clear in the region between latitudes –60° and +60°. For this region the difference is approximately linear and oscillates about $\beta = 0°$ with a period of one year. The difference itself can be fitted well to

$$\Delta S_{\mathrm{NR}}(\beta,t) = -285 \cdot \left(\beta/60^\circ\right) \cdot \sin\left(30^\circ t\right) \qquad (17)$$

(where t = 0, September 15; t = 1, October 15; etc.).

Now, we have shown that the annual average S_{NR} follows Eq. (16), and the difference between monthly and annual values follows Eq. (17), so the monthly S_{NR} can be written as

$$S_{\mathrm{NR}}^{\mathrm{fit}}(\beta,t) = 40 + 80\cos 2(\beta+\Delta) - 10\sin 6|\beta| + \Delta S_{\mathrm{NR}}(\beta,t) \qquad (18)$$

in the specified region $-60^\circ \le \beta \le +60^\circ$. For the month of January, the values of S_{NR} calculated directly from the data are compared to those given by Eq. (18) in Fig. 94.70. The fitting is very close to the calculated values in the region $-30^\circ \le \beta \le +45^\circ$. The discrepancies of up to 50 W/m^2 outside this region are most likely due to the hemispheric asymmetry of S_{NR}. This asymmetry was ignored in Eq. (17), which is antisymmetric about $\beta = 0^\circ$ and uses a perfectly sinusoidal maximum value for $\beta = \pm 60^\circ$. The calculations from data, however, show that during the southern summer, $S_{\mathrm{NR}}(-60^\circ,t)$ increases to close to 400 W/m^2, but in the northern summer $S_{\mathrm{NR}}(+60^\circ,t)$ does not even reach 300 W/m^2. Also, at any month, the value of $S_{\mathrm{NR}}(60^\circ,t)$ does not equal $S_{\mathrm{NR}}(-60^\circ,t)$, as in Eq. (17), leading to an over- or underestimation of S_{NR} from Eq. (18).

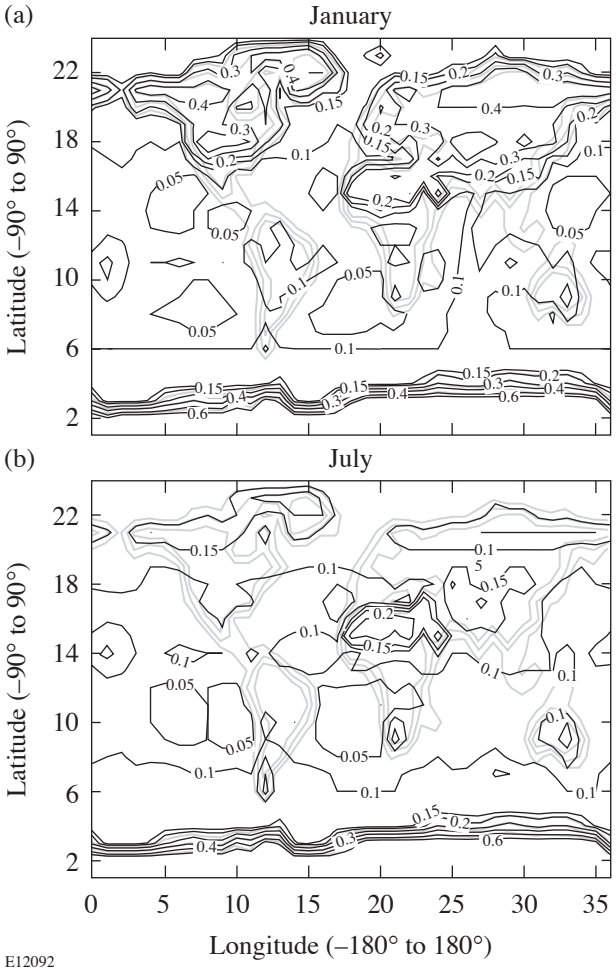

Figure 94.69
Comparison of surface reflectivities in the months of January (a) and July (b). The asymmetry between the northern and southern hemispheres seen in many climatological studies can be appreciated from the variability in the north polar region and the near-invariance in the south polar region. (See the caption of Fig. 94.64 for the key to the axes.)

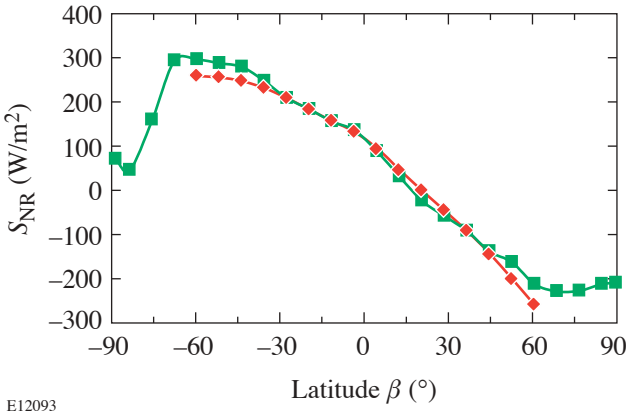

Figure 94.70
A sample determination of nonradiative flux S_{NR} for the month of January (18-year average). Diamonds: values determined from our model calculation. Squares: values determined from the fitting function, Eq. (18). The fit is meant to be valid for latitudes satisfying $-60^\circ \le \beta \le +60^\circ$.

Finally, in Fig. 94.71 we compare averages of S_{NR} over two months in succession (February and March 1995). The 18-year average for the respective months has been subtracted, and the polar regions have been omitted from the diagram because average monthly variations in reflectivities and cloud cover

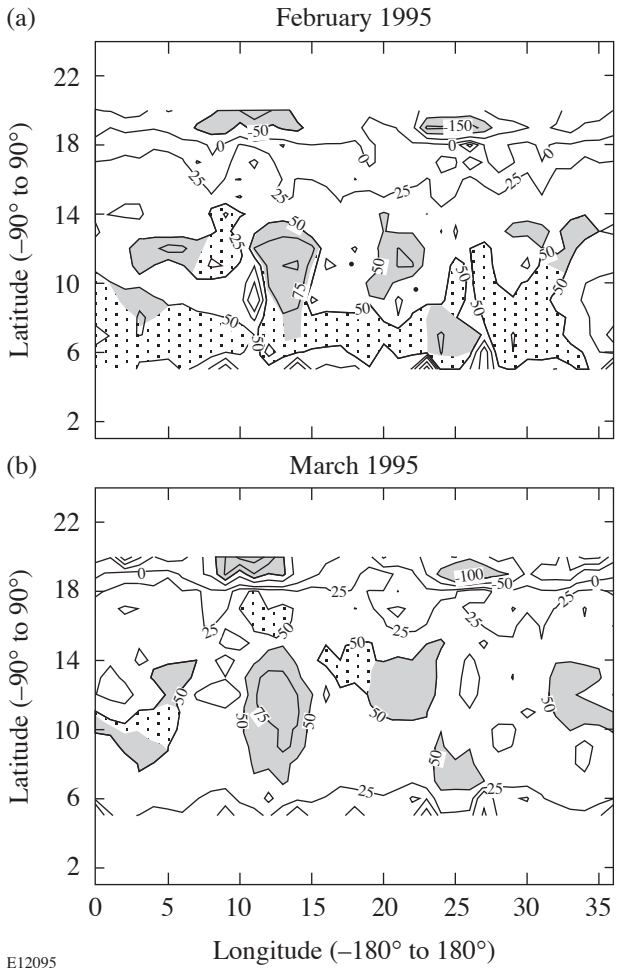

Figure 94.71
(a) The monthly values of S_{NR} for February 1995 minus the 18-year average value of S_{NR} for February, for the temperate zones. Large deviations, ~50 W/m^2, in large-scale "weather" patterns are seen. (b) Similar to (a), for March 1995. Comparing with February, it can be seen that some nonradiative "weather cells" (indicated by shading) persist for at least a month and some (indicated by stippling) are more ephemeral. The largest features cover 10 to 20 cells, each computed independently.

may be large. Deviations of the order of 50 W/m^2 show the presence of large-scale, persistent nonradiative "weather systems," each of which is composed of about 20 independent cells. These systems produce deviations in S_{NR} much larger than those shown in Fig 94.67(b). The figures serve to illustrate east–west nonradiative energy transport. Only when averages are taken over the 18-year database do the smooth results given by Eqs. (17) and (18) and Figs. 94.68 and 94.70 result.

Summary and Discussion

The two-level global model of Ref. 9 has been applied locally; that is, each cell in a grid has been assumed to have annual average temperatures and the fluxes have been determined by the cell's own parameters and average insolation. The observed local planetary albedo is used as a control on the modeled surface and atmospheric reflectivities. In the model's more successful (S_{NR}-predictive) implementation, the set of surface temperatures is used as input; the nonradiative flux from the surface S_{NR} and the ideal atmospheric radiative flux S_A are the principal outputs. The globally averaged S_{NR} is predicted to be about 64% of its usually quoted global value of 102 to 105 W/m^2, an improvement over T_E-predictive models using assumed nonradiative fluxes, where values of only 0%–40% were possible.

The value of the globally averaged atmospheric radiative flux S_A is 236 W/m^2, adequate to maintain overall radiative balance with an effective atmospheric radiative temperature of T_A = 254 K (recall that the emissivity is taken as 0.89, as in Ref. 9). Since our model assigns only this one temperature to the atmosphere, it is constrained to predict that the downward IR flux is identical to the upward flux. In the real atmosphere, a temperature gradient exists and the lower layers most effective in radiating downward are at a higher temperature. The downward flux should thus be greater than εS_A, as is observed.[18] We are developing a three-temperature version of our model, to be the subject of a future article in the series, and according to preliminary estimates, an appropriately larger value of S_{NR} will be obtained that will balance the extra downward IR.

Having noted a correlation between $S_{NR}(n)$ and latitude, we examined its zonal average. A clear asymmetry resulted between the northern and southern hemispheres, illustrating the effect of asymmetry of the hemispheric land masses and the differences in reflectivity parameters resulting from the nature of the Arctic and Antarctica. Fittings of other data sets to develop formulae for individual components of S_{NR} are discussed by Budyko.[5]

We emphasize the accessibility of both the data and our model representations to students interested in applying the elementary aspects of climatology to real data. As suggestions for future workers: (1) It would be interesting to use databases averaged over different periods of time to see if long-term differences in the form of Eqs. (17) and (18) result. (2) A study of the form, structure, and persistence of these large-scale

monthly "weather patterns" during an El Niño cycle should be informative.

ACKNOWLEDGMENT

We are grateful to Profs. D. Hartmann and K. Trenberth for valuable correspondence. This work was supported in part by NSF (REU) grant PHY 99-87413.

Appendix A: Spherical Astronomy Fundamentals

The altitude H of the sun can be found by applying the law of cosines[20] to the observer's spherical triangle ΔZNS, where Z is the observer's zenith, N is the north celestial pole, and S is the sun. Then arc ZS is $90°–H$; arc NZ is $90°–\beta$, where β is the latitude; and arc NS is $90°–\delta$, where δ is the *declination* of the sun, available from a table lookup in, e.g., Ref. 21.

List of symbols and abbreviations. [Note: symbols of the form $T_A(n)$ are not included. The meaning of such a symbol is "the value of T_A in cell n."

A	UV atmospheric input parameter [Eq. 2(a)]	r_{sea}	Reflectivity of the sea portion of a cell
$A(p)$	Area of a band of cells of latitude index p	S_0	Solar constant averaged globally and over time, 342 Wm^{-2}
$A(p,q)$	Area of a cell of latitude index p and longitude index q	S_A	Ideal radiative flux in the atmosphere or upper atmosphere layer, σT_A^4
a	Atmosphere's absorptivity in the UV	S_E	Ideal radiative flux in the surface layer, σT_E^4
a_{clear}	Absorptivity of cloudless air in the UV	S_{NR}	Net nonradiative flux upward from the surface
a_{cloud}	Absorptivity of air with clouds in the UV	t	Solar hour angle (see Appendix)
B	UV surface input parameter [Eq. 2(b)]	T'	Time elapsed since the vernal equinox
f_{cloud}	Fraction (of a cell area) consisting of cloud	T_A	Effective radiative temperature of the upper model layer, representing that of the atmosphere
f_{land}	Fraction (of a cell area) consisting of land	T_E	Temperature of the lower model layer, representing that of the surface of Earth
H	Horizon angle of the sun	UV	Refers to that part of the spectrum of the sun that is absorbed by the atmosphere; roughly wavelengths shorter than 600 nm
IR	Refers to that part of the spectrum with wavelengths longer than 600 nm; largely not absorbing the sun's spectrum but absorbing much of Earth's	α_P	Planetary albedo
k_M	Multiple reflection parameter	β	Latitude associated with a set of cells
n	Cell label, also in matrix style p, q	δ	Solar declination angle
p, q	Latitude and longitude cell indexes, respectively	Δ	Fitting parameter (phase shift); see **Summary and Discussion**.
r_A	Reflectivity of the atmosphere in the UV	ε	Atmosphere's absorptivity (and emissivity) in the IR
r_{clear}	Reflectivity of clear air	ε_{clear}	Clear air absorptivity (and emissivity) in the IR
r_{cloud}	Reflectivity of the cloud portion of a cell	ε_{cloud}	Cloud absorptivity (and emissivity) in the IR
r_{land}	Reflectivity of the land portion of a cell	σ	Stefan–Boltzmann constant, 5.67×10^{-8} Wm^{-2} K^{-4}
r_S	Reflectivity of the surface in the UV		

The angle $\angle SNZ$ is called the sun's *hour angle H*; instead of being measured in degrees, it is measured in time units from 12:00 noon (1 h = 15°). It is negative (positive) when the sun is in the eastern (western) half of the sky. These quantities are related by the spherical law of cosines:

$$\sin H = \sin\beta \sin\delta + \cos\beta \cos\delta \cos t, \qquad \text{(A1)}$$

At sunrise, $H = 0$; the equation determines the time at sunrise $t = -t_0$. At sunset, again $H = 0$ and $t = +t_0$. The length of daylight is then $2t_0$.

The declination of the sun can also be approximated. The sun moves along a great circle, called the *ecliptic*, which is inclined at an angle $i = 23.44°$ to the celestial equator. At the vernal equinox (~March 21) the sun is at a point *V*, one of the two intersections of the celestial equator and the ecliptic, and is moving from negative to positive declination. Let the point *P* be on the celestial equator, with arc $NSP = 90°$. Consider the spherical triangle *VSP*. The angle $\angle SVP = i$ and the angle $\angle SPV = 90°$. The arc *VS* is *approximately* $\Omega t'$, where $\Omega = 360°/1$ yr and t' is the time elapsed since the vernal equinox. From the spherical law of sines for *VSP* one has

$$\sin\delta = \sin i \sin\Omega'. \qquad \text{(A2)}$$

Since the sun moves slightly faster (slower) on the ecliptic than average when we are at perihelion, January (aphelion, July), this is only an approximate relation.

REFERENCES

1. J. Hansen *et al.*, Proc. Natl. Acad. Sci. USA **97**, 9875 (2000).
2. D. L. Hartmann, *Global Physical Climatology*, International Geophysics, Vol. 56 (Academic Press, San Diego, 1994).
3. J. P. Peixoto and A. H. Oort, *Physics of Climate* (American Institute of Physics, New York, 1992).
4. M. I. Budyko, Tellus **21**, 611 (1969).
5. M. I. Budyko, *The Earth's Climate, Past and Future*, International Geophysics Series, Vol. 29 (Academic Press, New York, 1982).
6. K. E. Trenberth, J. M. Caron, and D. P. Stepaniak, Clim. Dyn. **17**, 259 (2001).
7. K. E. Trenberth and J. M. Caron, J. Clim. **14**, 3433 (2001).
8. C. Kittle and H. Kroemer, *Thermal Physics*, 2nd ed. (W. H. Freeman, San Francisco, 1980), pp. 115–116.
9. R. S. Knox, Am. J. Phys. **67**, 1227 (1999).
10. S. Arrhenius, Phil. Mag. **41**, 237 (1896).
11. J. R. Barker and M. H. Ross, Am. J. Phys. **67**, 1216 (1999).
12. J. Hansen *et al.*, Mon. Weather Rev. **111**, 609 (1983).
13. G. J. Borse, *Numerical Methods with MATLAB®: A Resource for Scientists and Engineers* (PWS Publishing, Boston, 1997).
14. C. Brest (technical contact), "ISCCP D2 Monthly Means and Climatology," data sets retrieved 21 January 2002 from the International Satellite Cloud Climatology Project, available at http://isccp.giss.nasa.gov/products/browsed2.html.
15. The ISCCP data for r_S was not used in regions above ±52° latitude because the data sometimes are greater than unity as a result of glaring and the angle of the satellite to the northern and southern polar regions. This being inconsistent with our definition of a reflection coefficient, the surface reflectivities in these regions were estimated from the Hartmann[2] Table 4.2.
16. J. T. Kiehl and K. E. Trenberth, Bull. Am. Meteorol. Soc. **78**, 197 (1997).
17. See M. I. Budyko, *The Earth's Climate, Past and Future*, International Geophysics Series, Vol. 29 (Academic Press, New York, 1982), p. 70.
18. R. E. Dickinson, in *Climate System Modeling*, edited by K. E. Trenberth (Cambridge University Press, Cambridge, England, 1992), Chap. 5, pp. 149–171.
19. See D. L. Hartmann, *Global Physical Climatology*, International Geophysics, Vol. 56 (Academic Press, San Diego, 1994), pp. 152–154.
20. W. M. Smart, *Text-Book on Spherical Astronomy* (Cambridge University Press, Cambridge, England, 1947).
21. R. Gupta, ed. *Observer's Handbook* (The Royal Astronomical Society of Canada, Toronto, 2002).